Research
Materials for Molecular Separations—Article

Guest Solvent-Directed Isomeric Metal–Organic Frameworks for the Kinetically Favorable Separation of Carbon Dioxide and Methane

Dan Lai [a,#], Fuqiang Chen [a,#], Lidong Guo [a], Lihang Chen [a], Jie Chen [a], Qiwei Yang [a,b], Zhiguo Zhang [a,b], Yiwen Yang [a,b], Qilong Ren [a,b], Zongbi Bao [a,b,∗]

[a] Key Laboratory of Biomass Chemical Engineering of the Ministry of Education, College of Chemical and Biological Engineering, Zhejiang University, Hangzhou 310027, China
[b] Institute of Zhejiang University–Quzhou, Quzhou 324000, China

ARTICLE INFO

ABSTRACT

The adsorptive separation of CH_4 from CO_2 is a promising process for upgrading natural gas. However, thermodynamically selective adsorbents exhibit a strong affinity for CO_2 and thus require a high energy compensation for regeneration. Instead, kinetic separation is preferred for a pressure swing adsorption process, although precise control of the aperture size to achieve a tremendous discrepancy in diffusion rates remains challenging. Here, we report a guest solvent-directed strategy for fine-tuning the pore size at a sub-angstrom precision to realize highly efficient kinetic separation. A series of metal–organic frameworks (MOFs) with isomeric pore surface chemistry were constructed from 4,4′-(hexafluoroisopropylidene)-bis(benzoic acid) and dicopper paddlewheel notes. The resultant CuFMOF·CH_3OH (CuFMOF-c) exhibits an excellent kinetic separation performance thanks to a periodically expanding and contracting aperture with the ideal bottleneck size, which enables the effective trapping of CO_2 and impedes the diffusion of CH_4, offering an ultrahigh kinetic selectivity (273.5) and equilibrium-kinetic combined selectivity (64.2). Molecular dynamics calculations elucidate the separation mechanism, and breakthrough experiments validate the separation performance.

1. Introduction

Natural gas, which primarily consists of methane (CH_4), will grow to account for a quarter of the global energy demand in the coming decades [1–3]. Nevertheless, the abundant low-quality natural gas, which has a medium concentration of CH_4 mixed with basically equivalent amounts of carbon dioxide (CO_2), cannot meet the demand for industrial applications [4–6]. Consequently, the CO_2 must be removed to improve the combustion efficiency and prevent equipment and pipeline corrosion during transportation [7–13]. At present, the mature industrial technology of CO_2 removal involves amine scrubbing, which is costly due to the huge energy input required for absorbent regeneration and is susceptible to oxidative and thermal degradation [14–17].

Adsorbent-based separation processes have been proposed as an alternative technology with a lower regeneration energy, higher efficiency, and easier operation [18–30]. However, porous adsorbents such as zeolites and amine-functionalized silicas still show high adsorption enthalpies for CO_2, despite demonstrating remarkable thermodynamic selectivity [31–34]. Instead, kinetic separation based on a difference in diffusion rate is preferred if the adsorbents are hydrophobic and show significant kinetic selectivity. For example, carbon molecular sieves (CMSs) can purify natural gas based on kinetic separation, with an adsorption heat of CO_2 as low as 10.9 kJ·mol^{-1} [35,36]. Nonetheless, it remains challenging to precisely control the micropores of carbon adsorbents by means of carbonization in order to manipulate the kinetic selectivity of CO_2/CH_4 [37–39].

Versatile metal–organic frameworks (MOFs) could serve as an ideal platform to meet the strict prerequisites for kinetic separation due to their structural diversity and pore size fine-tunability [40–54]. For example, Lee et al. [55] demonstrated the efficient kinetic separation of propylene/propane in isostructural zinc-pillared-paddlewheel MOFs by controlling the pore apertures and the rectangular-plate morphology of the crystals. Similarly, Lyndon et al. [56] proposed a mixed-linker strategy for fine-tuning

∗ Corresponding author.
E-mail address: baozb@zju.edu.cn (Z. Bao).
# These authors contributed equally to this work.

structurally flexible apertures (~3 Å, 1 Å = 10^{-10} m), which facilitates the selective diffusion of ethylene over ethane. Recently, Gu et al. [57] presented a copper (Cu)-based MOF in which flip-flop molecular motions within the framework structure provide kinetic gate functions that enable the efficient separations of oxygen/argon and ethylene/ethane. Nevertheless, few efforts have been devoted to construct MOFs for the kinetic separation of CO_2/CH_4, partially due to the difficulty of fabricating an appropriate aperture with sub-angstrom precision, and partially because of the close kinetic diameters of CO_2 (3.3 Å) and CH_4 (3.8 Å).

Herein, we report a guest solvent-directed isomeric micropore-tuning strategy within a ultra-microporous Cu(hfipbb)-$(H_2hfipbb)_{0.5}$ (where $H_2hfipbb$ is 4,4′-(hexafluoroisopropylidene)-bis(benzoic acid)), termed CuFMOF-a, for the kinetic separation of CO_2/CH_4. As the parent, CuFMOF-a exhibits a periodically expanding and contracting aperture with a bottleneck size of 3.2 Å × 3.5 Å that hinders the diffusion of CH_4. Its offspring, CuFMOF·CH_3OH (termed CuFMOF-c), which has a similar pore surface and an aperture size increased by 0.2 Å, facilitates the diffusion of CO_2 but prevents the diffusion of CH_4, with an unprecedented kinetic selectivity. CuFMOF·DMF (termed CuFMOF-b; DMF is short for N,N-dimethylformamide), which has an aperture size that is further increased by 0.2 Å, promotes the diffusion of both CO_2 and CH_4, which diminishes the kinetic separation of CO_2/CH_4. Moreover, CuFMOF-c shows a moderate thermodynamic selectivity of CO_2 over CH_4; thus, the synergetic equilibrium-kinetic effect boosts the efficient breakthrough separation of a CO_2/CH_4 gas mixture. Grand canonical Monte Carlo (GCMC) and molecular dynamics (MD) simulations further demonstrate the critical role of pore-size tuning for kinetic separation.

2. Experimental section

2.1. Materials

The organic ligand $H_2hfipbb$ (98%) was obtained from TCI (China). Copper chloride dihydrate ($CuCl_2·2H_2O$, 99.99%) and copper nitrate trihydrate ($CuNO_3·3H_2O$, 99%) were purchased from Aladdin (China) and Macklin (China), respectively. Carbon dioxide (99.999%), methane (99.999%), helium (99.999%), and mixed gases CH_4/CO_2 (50/50, v/v) were customized from Jingong Co., Ltd. (China). All chemicals were obtained from commercial sources and were used as received without further purification.

2.2. Synthesis of CuFMOF-a

The synthesis of CuFMOF-a followed the previously reported procedure by Pan et al. [58]. Excess $H_2hfipbb$ (729 mg, 1.86 mmol) with $Cu(NO_3)_2·3H_2O$ (145 mg, 0.6 mmol) and 30 mL deionized water were heated at 150 °C for 12 h to obtain blue columnar crystals. After cooling to room temperature, the product was washed with DMF to remove excess H_2fipbb; it was then washed with deionized water and finally dried in air.

2.3. Synthesis of CuFMOF-b

The organic linker $H_2hfipbb$ (235.4 mg, 0.6 mmol) and Cu$(NO_3)_2·3H_2O$ (145 mg, 0.6 mmol) were dissolved in a mixture of DMF (36 mL) and deionized water (12 mL). The solution was heated in an autoclave at 65 °C for 48 h to obtain blue crystals. The product was washed with DMF (30 mL) three times and then with methanol (30 mL) three times, and was finally dried at room temperature.

2.4. Synthesis of CuFMOF-c

The organic linker $H_2hfipbb$ (117.7 mg, 0.3 mmol) and $CuCl_2·2H_2O$ (51.2 mg, 0.3 mmol) were dissolved in a mixture of DMF (14 mL) and methanol (14 mL) and acidified with 0.1 mol·L^{-1} HCl (0.7 mL) to yield the product. The solution was heated in an autoclave at 80 °C for 24 h to obtain blue petal-like crystals. The product was washed with DMF (30 mL) three times and then with methanol (30 mL) three times. Finally, it was dried at room temperature.

2.5. Gas adsorption measurements

To remove all the guest solvent in the framework, the CuFMOF-c sample (~300 mg) was degassed at 120 °C for 24 h prior to measurements. CO_2 and CH_4 adsorption isotherms were measured on a Micromeritics ASAP 2460 (Micromeritics Instrument Corp., USA). The Brunauer–Emmett–Teller (BET) surface areas of CuFMOF-c and CuFMOF were characterized by CO_2 adsorption–desorption isotherms at 195 K.

2.6. Adsorption kinetics measurements

The kinetic adsorption profiles were measured on an Intelligent Gravimetric Analyzer (IGA001, Hiden, UK), which uses a gravimetric technique to accurately measure the transient gas uptake as a function of time under various operating conditions. For each test, about 120 mg of MOF sample was loaded into the sample basket; then, the system was outgassed at 393 K for 8 h prior to the dynamic gas sorption measurements. The adsorption kinetics were obtained by measuring the mass change at a given temperature at 100 mbar (1 mbar = 10^{-3} bar = 100 Pa), and the pressure was boosted up by introducing the target gas into sample chamber from 0 to 100 mbar at 200 mbar·min^{-1}. The adsorption kinetics were collected at various temperatures from 278 to 318 K. After each test, the chamber was backfilled with the target gas to 1000 mbar, and the sample was replaced by the new sample for the next test. All the gases used (CH_4, CO_2, and He) were of ultra-high purity (99.999%).

2.7. Dynamic breakthrough experiments and desorption experiments

The breakthrough experiments for the CO_2/CH_4 (50/50, v/v) mixtures were carried out at a flow rate of about 2.5 mL·min^{-1} (298 K, 1.01 bar). Activated MOF particles (CuFMOF-a, 1.317 g; CuFMOF-b, 1.053 g; CuFMOF-c, 1.172 g) were packed into a ϕ4.6 mm × 100 mm stainless steel column under a nitrogen (N_2) atmosphere. After each breakthrough experiment, the adsorption bed was regenerated by helium flow with a rate of 20 mL·min^{-1} at 298 K for 30 min. Based on the mass balance, the gas adsorption capacities can be determined as follows:

$$q_i = \frac{C_i V}{22.4 \times m} \times \int_0^t \left(1 - \frac{F}{F_0}\right) dt \tag{1}$$

where q_i is the equilibrium adsorption capacity of gas i (mmol·g^{-1}), C_i is the feed gas concentration, V is the volumetric feed flow rate (mL·min^{-1}), t is the adsorption time (min), F_0 and F are the inlet and outlet gas molar flow rates, respectively, and m is the mass of the adsorbent (g).

2.8. Density functional theory calculations

First-principles density functional theory (DFT) calculations were performed using the Materials Studio's CASTEP code.47. Vanderbilt-type ultrasoft pseudopotentials and the generalized

gradient approximation (GGA) with the Perdew–Burke–Ernzerhof (PBE) exchange correlation were used for all structure geometry optimization calculations. A cutoff energy of 544 eV and a $3 \times 3 \times 2$ k-point mesh were found to be sufficient for the total energy to converge within 0.05 MeV per atom. The optimized structures were consistent with the experimentally determined crystal structure of the coordination networks.

2.9. GCMC and MD simulation

We performed adsorption and diffusion simulations of CO_2 and CH_4 in CuFMOF-a, CuFMOF-b, and CuFMOF-c using GCMC [59] and MD, respectively. All simulations were performed at room temperature using a rigid MOF structure with atomic positions obtained from experimental data. A simulation volume of $2 \times 2 \times 2$ crystallographic unit cells was used for all simulations. Assuming that the MOF is rigid greatly reduces the complexity of defining interatomic potentials for these simulations, as well as their computational efficiency. CH_4 was modeled as a spherical Lennard–Jones (LJ) particle [60], while CO_2 was modeled as a rigid three-site molecule using the elementary physical model-2 (EPM2) [61] and as an all-atom model with LJ potentials and atomic charges to approximate the quadrupole moment of CO_2. A comparison of the experimental adsorption isotherms (Fig. S1 in Appendix A) with the simulated adsorption isotherms (Fig. S2 in Appendix A) revealed that the simulated adsorption data is slightly higher than that of the experimental adsorption. However, under ideal circumstances, it will be slightly higher than the actual data, due to the existence of cell defects and other problems. Thus, the parameters work well for CO_2 and CH_4, indicating that the parameters used are reasonable.

The Lorentz–Berthelot mixing rules were employed to calculate the adsorbate–MOF LJ cross-interaction parameters by using the universal force field (UFF) [62] for the framework atoms. The charges on an atom in the MOF were determined by means of dispersion-corrected density functional theory (DFT-D) calculations with Accelrys DMol^3 in the Materials Studio package. DFT calculations were conducted under the GGA with a PBE and double numerical plus polarization (DNP) basis set. A semi-empirical dispersion correction was included in the calculation to account for van der Waals interactions. The space cut-off radius (4.0 Å) and a $2 \times 2 \times 2$ k-point mesh were used for geometry optimization, and a convergence tolerance with a fine quality was employed in the calculations. We used MD to compute the self-diffusion coefficient of CO_2. MD was performed in the canonical ensemble with a Nose–Hoover thermostat [63] for a time of 20 ns for each loading and/or composition we considered. Initial states were created using GCMC. The self-diffusion calculation is based on the Einstein equation:

$$D_s(c) = \frac{1}{2dN_m} \lim_{t \to \infty} \frac{d}{dt} \langle \sum_{j=1}^{N_m} |r_j(t) - r_j(0)|^2 \rangle \qquad (2)$$

where c is the concentration of the adsorbate molecules, d is the dimension of system space, N_m is the number of molecules in the system, and $r_j(t)$ is the displacement of the labeled particle j at time t.

3. Results and discussion

3.1. Synthesis and characterization of MOFs

CuFMOF was successfully synthesized according to a previously reported method [58]. As demonstrated by single-crystal X-ray diffraction analysis, CuFMOF-a was further expanded into a three-dimensional (3D) framework structure by connecting the

carboxylic acid hfipbb^{2-} ligand at the apical position of six connected nodes (Fig. 1(a)). Each bent shape of the hfipbb^{2-} ligand of these materials adopts a spiral extension to link the upper and lower layers, which constructs a structure that periodically outspreads and contracts the cross-section of the channel (Fig. 1(b)). Consequently, the channel can be described as a narrow bottleneck structure interconnected by an iterant cage space.

The pore size was measured to be 3.5 Å, which is slightly larger than the kinetic diameter of CO_2 (3.3 Å) and smaller than that of CH_4 (3.8 Å). Given that the solubility of the organic ligand of CuFMOF-a in water is quite low, DMF was added to dissolve the ligand. Surprisingly, a new form of crystal MOF, denoted as CuFMOF-b, was obtained. Unlike the structure of the parent, CuFMOF-a, the paddlewheel copper atoms in CuFMOF-b act as a four-connected node that connects the four bent shapes of the ligands located in the equatorial plane, while the apical positions of the nodes connect to the DMF, forming a single-layer network in the ac-plane (Fig. 1(c), Table S1 in Appendix A).

Interestingly, the chiral pores of CuFMOF-b are formed by entangled left-handed spiral double strands, while those of CuFMOF-a are formed by entangled right-handed spiral double strands. Notably, the bending angles of the V-shaped hfipbb^{2-} within CuFMOF-a (72.8°) are slightly larger than those of CuFMOF-b (71.8°) due to the different coordination structure of the top linker of the copper square pyramidal shape (Figs. 1(b) and (d)), thus giving CuFMOF-b a subtly larger channel bottleneck with a pore size of 3.9 Å. Similarly, another MOF with an isomeric pore surface, denoted as CuFMOF-c, was fabricated for the first time by replacing water with methanol as the guest solvent (Fig. 1(e), Table S1). As evidenced by single-crystal analysis, the as-synthesized CuFMOF-c is crystallized in the *Pccn* space group and features an isomeric chiral pore structure formed by entangled left-handed spiral double strands, like those of CuFMOF-b, although the bending angle is smaller and the bottleneck of the channel is reduced to 3.7 Å (Fig. 1(f)). This alteration may originate from the different coordinated solvent molecules associated with the axial position of the copper atoms; thus, it influences the supramolecular arrangement of the MOF layers. To further demonstrate the role of the coordinated solvent molecules in tuning the isomeric pore structure, single-crystal X-ray diffraction tests were performed of the activated MOFs. It was found that the solvent molecules were still firmly coordinated with the copper atoms after activation in a vacuum at 120 °C for 24 h (Table S2 in Appendix A).

The ultra-microporous structure of these MOFs was verified by CO_2 adsorption tests at 195 K, which revealed the typical characteristics of micropores, as seen from the steep increase of the isotherms within the relative pressure range of 0.01 (Fig. S3 in Appendix A). It is worth noting that the steep increase of the isotherms at a relative pressure from 0.7 to 0.8 on CuFMOF-b and CuFMOF-c may be caused by the agglomeration of MOFs. The BET specific surface areas were calculated to be 56.4, 126.4, and 82.6 m$^2 \cdot$g^{-1} for CuFMOF-a, CuFMOF-b, and CuFMOF-c, respectively.

3.2. Static adsorption tests and kinetic adsorption experiments

Inspired by the appropriate pore size and well-developed porosity, adsorption isotherms of CO_2 and CH_4 were collected (Fig. 2(a) and Fig. S1). As shown in Fig. 2(a), CuFMOF-c displays the highest CO_2 uptake of 0.93 mmol·g^{-1} at 298 K and 100 kPa, surpassing those of CuFMOF-a (0.64 mmol·g^{-1}) and CuFMOF-b (0.80 mmol·g^{-1}), which is consistent with the order of the BET specific surface areas. In addition, the CH_4 uptake decreases from 0.58 to 0.31 mmol·g^{-1} when going in order from CuFMOF-c to CuFMOF-a, which is lower than that of CO_2, demonstrating the
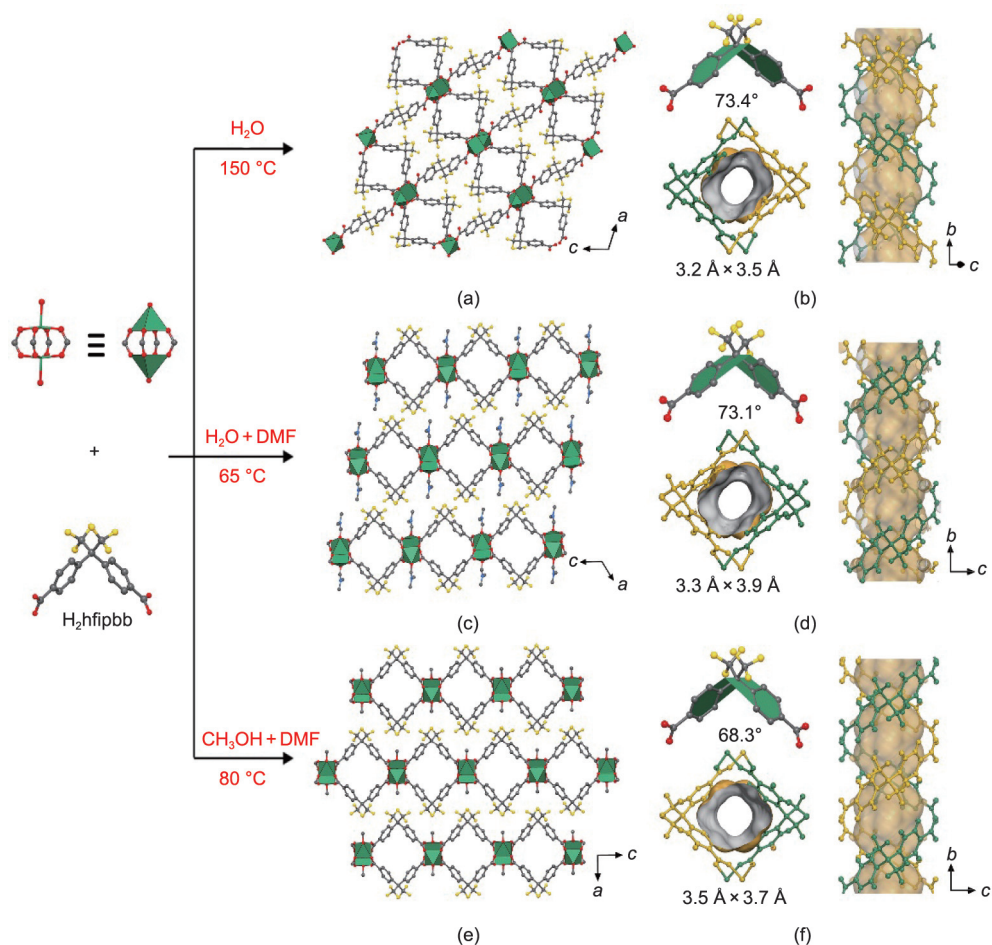
Fig. 1. Schematic representation of the synthesis of CuFMOF-a, CuFMOF-b, CuFMOF-c, and their corresponding structures. The crystal structure of the as-synthesized (a) CuFMOF-a, (c) CuFMOF-b, and (e) CuFMOF-c along the *b*-axis showing the one-dimensional (1D) channels. The dihedral angle of the bent-shape hfipbb^{2-} ligand and the Connolly surface indicate the periodic expansion and contraction of the cross-section of the channel in (b) CuFMOF-a, (d) CuFMOF-b, and (f) CuFMOF-c. The nets are highlighted in dark green for clarity. Color code: Cu (green), F (yellow), C (gray), O (red), N (blue); H atoms are omitted for clarity.

weaker affinity between CH_4 molecules and the MOF structure. The Henry's selectivities of CO_2/CH_4 were calculated to be 5.0, 3.2, and 2.9 for CuFMOF-a, CuFMOF-b, and CuFMOF-c, respectively, which are slightly lower than that of 5A (Sinopec) zeolite (7.8) [64] and Bergbau–Forschung (BF)-CMS (5.2) [35]. The isosteric heat of adsorption (Q_{st}) was calculated based on single-component isotherms collected at 278, 298, and 318 K, by using the Clausius–Clapeyron equation and Langmuir–Freundlich model (Fig. S2 and Tables S3–S5 in Appendix A). The optimal CuFMOF-c exhibits a moderate Q_{st} for CO_2 and CH_4 with respective values of 21.97 and 17.66 kJ·mol^{-1} at zero coverage, indicating its easy generation and great potential in practical energy-saving applications.

The delicate structure of these MOFs inspired us to evaluate their CO_2/CH_4 kinetic separation performance. Time-dependent kinetic adsorption isotherms of CO_2 and CH_4 were measured at various temperatures ranging from 278 to 318 K (Figs. 2(b) and (c), Fig. S4 in Appendix A). As expected, all MOFs showed a considerably faster diffusion rate for CO_2 than for CH_4 over the whole temperature range. The adsorption of CO_2 in CuFMOF-b and CuFMOF-c reached equilibrium within 5 min at 298 K and 100 mbar (Fig. 2(b)). In contrast, CuFMOF-a exhibited the lowest diffusion rate of CO_2 because it has the narrowest pore size, and did not reach equilibrium until 30 min under identical conditions. As for CH_4 diffusion, the fastest diffusion rate was observed for CuFMOF-b due to its further increased pore size at the bottleneck. The quantity of CH_4 adsorption for CuFMOF-a and CuFMOF-c still

did not reach an equilibrium state after 60 min and kept climbing up gradually. Therefore, the difference in the diffusion behavior of CO_2 and CH_4 was the greatest for CuFMOF-c.

To achieve a better quantitative comparison of the diffusion rate, we adopted the classic micropore diffusion mode [65] to quantify the kinetic selectivity. The diffusion time constants (D_c/r_c^2, where D_c is the intracrystalline diffusivity, and r_c is the radius of the equivalent spherical particle) for CO_2 and CH_4 were calculated, from which the kinetic selectivity could be obtained (Tables S6 and S7 in Appendix A). CuFMOF-a, which has the smallest pore size, exhibited an inconspicuous difference in the adsorption kinetics of CO_2 and CH_4. CuFMOF-a showed diffusion time constants of 1.950×10^{-4} and 1.215×10^{-5} s^{-1} for CO_2 and CH_4 at 298 K, respectively, giving a CO_2/CH_4 kinetic selectivity of merely 16.1, because not only is the diffusion of CH_4 restricted when it diffuses from one center cage through the bottleneck to another adjacent center cage, but the diffusion of CO_2 is also restricted due to the too-narrow pore size. Nevertheless, CuFMOF-b, which features the largest pore size, presents a kinetic selectivity of CO_2/CH_4 (36.1), with the diffusion time constant of CH_4 dramatically increasing to 7.31×10^{-5} s^{-1} and that of CO_2 slightly increasing to 2.64×10^{-3} s^{-1} at 298 K. Notably, the diffusion time constants of CO_2 and CH_4 at 298 K on CuFMOF-c were calculated to be 1.803×10^{-3} and 1.795×10^{-5} s^{-1}, offering a dramatic CO_2/CH_4 kinetic selectivity of up to 100.5. These observations can be elucidated qualitatively by the size of the narrow bottleneck, which
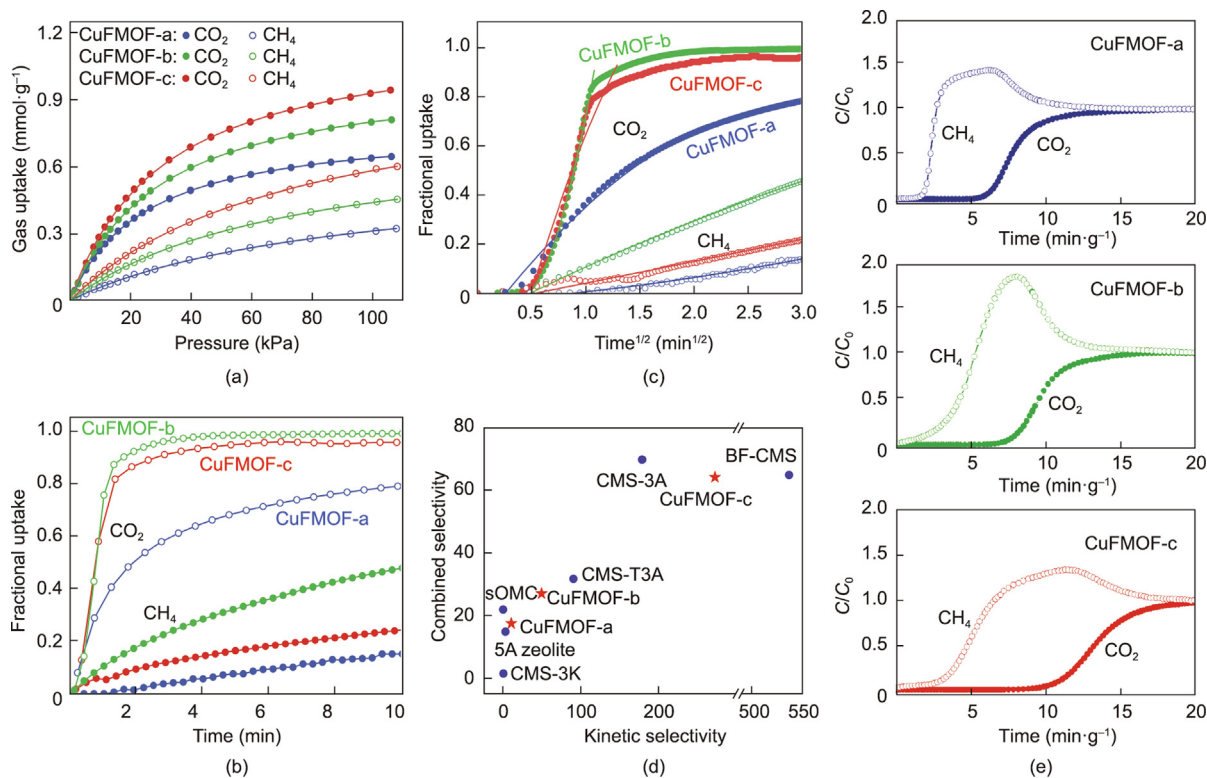
Fig. 2. (a) Single-component adsorption isotherms of CO_2 and CH_4 for CuFMOF-a (blue), CuFMOF-b (green), and CuFMOF-c (red) at 298 K; the solid lines represent the fitting curves via the Langmuir equation, and the solid dots and circles represent experimental data. (b, c) Time-dependent gas uptake profiles of CO_2 and CH_4 for CuFMOF-a (blue), CuFMOF-b (green), and CuFMOF-c (red) at 298 K and 100 mbar at different time scales. (d) Performance comparison of various adsorbents on CO_2/CH_4. (e) Experimental column breakthrough curves for a binary mixture of CO_2/CH_4 (50/50, v/v) at 298 K and 1 bar with a flow of 2.5 mL·min^{-1}. The ordered mesoporous carbon obtained after the removal of silica was referred as sOMC. C is the outlet gas concentration, and C_0 is the outlet gas concentration at equilibrium.

naturally facilitates the diffusion of the smaller CO_2 molecules while setting a barrier that prevents the larger CH_4 molecules from diffusing in the channel. Compared with CuFMOF-a and CuFMOF-b, the pore size in CuFMOF-c (3.7 Å) is an optimal aperture for the kinetic separation of CO_2 and CH_4, as it is large enough for CO_2 to diffuse into but smaller than the kinetic diameter of CH_4, resulting in a high kinetic selectivity of CO_2/CH_4. These results indicate that structural pore size tuning via solvent substitution is a promising strategy for kinetic separation.

It is worth noting that the diffusion rate steadily decreases with decreasing temperature, with the diffusion rate of CH_4 being more significantly affected by temperature than that of CO_2. When the temperature was further decreased to 278 K, a remarkably high kinetic selectivity of CO_2/CH_4 (273.5) was obtained on CuFMOF-c, which is significantly higher than that of other reported kinetically selective adsorbents such as CMS-3K (1.1) [66], CMS-T3A (91.7) [67], BF-CMS (180) [35], and 5A zeolite (3.6) [64], and comes second only to CMS-3A (537.3) [35] (Table S7). The diffusion activation energy of CO_2 and CH_4 were calculated using the Arrhenius equation (see Appendix A). The significantly higher diffusion activation energy of CH_4 in comparison with that of CO_2 further demonstrates the high selectivity of CO_2 over CH_4 on these MOFs (Table S8 in Appendix A). The equilibrium-kinetic combined selectivity [68], which is an important parameter to evaluate the performance of adsorbents, was also calculated and compared. As displayed in Fig. 2(d) and Table S7, a dramatically high combined selectivity (64.2) was achieved on CuFMOF-c, outperforming that of most reported adsorbents and even being comparable to those of commercial CMSs such as CMS-3A (64.9) [35] and BF-CMS (69.8) [35]. This finding indicates the great potential of CuFMOF-c for CO_2/CH_4 separation.

3.3. Breakthrough experiments and the MOFs' stability

To investigate the potential of these MOFs for CO_2/CH_4 in an actual separation process, real-time dynamic breakthrough experiments were conducted. CH_4 was first eluted within 2 min·g^{-1}, whereas CO_2 was retained on CuFMOF-c until 10 min·g^{-1}. This was followed by a retention time on CuFMOF-b of 7 min·g^{-1} and on CuFMOF-a of 5 min·g^{-1}. The dynamic uptake of CO_2 was calculated to be 0.50, 0.58, and 0.76 mmol·g^{-1}, respectively, for CuFMOF-a, CuFMOF-b, and CuFMOF-c, which is consistent with the results of the aforementioned static adsorption tests (Fig. 2(e)). Moreover, high-purity CH_4 (>99%) was obtained with a calculated productivity of 0.22, 0.18, and 0.24 mmol·g^{-1} for CuFMOF-a, CuFMOF-b, and CuFMOF-c, respectively.

Multiple breakthrough experiments were performed, and it was observed that there was no obvious decay in the dynamic adsorption uptake of CO_2 after 5 cycles (Figs. S5(a)–(c) in Appendix A), which demonstrates the excellent recyclability of these MOFs for CO_2/CH_4 separation. The desorption curves obtained by using helium to purge the column after the breakthrough experiments were also collected (Figs. S5(d)–(f) in Appendix A), and indicated the easy generation of adsorbents under mild ambient conditions.

Concerns about the stability of the adsorbents were also raised. The thermal stability of these MOFs was examined by means of thermogravimetric analysis (TGA; Fig. S6 in Appendix A). It was found that CuFMOF-a, CuFMOF-b, and CuFMOF-c are highly thermally stable up to 563, 548, and 488 K, respectively. Powder X-ray diffraction (PXRD) patterns of these MOFs under different conditions were also collected (Fig. S7 in Appendix A). After soaking the MOFs in water for 24 h and exposing them to air for a month, no loss of crystallinity was observed, showing the robust

chemical stability of these MOFs due to the hydrophobic characteristics of the fluorine-containing ligand.

3.4. GCMC and MD simulations

To structurally elucidate how CO_2 and CH_4 diffuse in the one-dimensional (1D) channel, GCMC and MD simulations were carried out. The GCMC simulation of the adsorption isotherms (Fig. S8 in Appendix A) matches well with the experimental results. As shown in Figs. 3(a)–(c), when each cell contains two gas molecules, the self-diffusion coefficients of the single-component CO_2 are calculated to be 1.2×10^{-6}, 1.19×10^{-5}, and 1.51×10^{-5} cm²·s⁻¹ for CuFMOF-a, CuFMOF-c, and CuFMOF-b, respectively, following the order of the diffusion rate of CO_2 obtained from the kinetic adsorption tests. It is noteworthy that the self-diffusivity of CO_2 decreases with increased loading. However, CH_4 cannot pass through the narrow bottleneck between adjacent capacious cage space on the nanosecond timescales available using MD, which is consistent with the results reported by Watanabe et al. [69].

The difference in the minimum potential energy of CO_2 and CH_4 (Figs. 3(d)–(f)), which is obtained by calculating the energy when a molecule is moved along a 1D channel of MOFs at each point, is the intrinsic reason for the disparity in the diffusion rates. The minimum energy occurs at the center of the capacious cage space, where CH_4 and CO_2 molecules are mainly accommodated (Fig. S9 in Appendix A). The diffusion energy barriers of CH_4 and CO_2 in CuFMOF-a were measured to be 69.8 and 22.4 kJ·mol⁻¹ (Fig. 3(d)), respectively, reflecting CuFMOF-a's slowest diffusion rate. As the pore size increases, the diffusion energy barriers of CH_4 and CO_2 decrease to 55.6 and 15.4 kJ·mol⁻¹, respectively, in CuFMOF-c (Fig. 3(f)). As for CuFMOF-b, which has the largest pore size, the diffusion energy barriers of CH_4 and CO_2 were estimated

to be 38.4 and 16.7 kJ·mol⁻¹ (Fig. 3(e)), respectively, indicating that these molecules can pass through the channel more easily. However, the insignificant difference between the movement of CH_4 and CO_2 in CuFMOF-b results in a lower kinetic selectivity for CO_2/CH_4 separation. Therefore, CuFMOF-c is shown to have the most suitable pore size for the kinetic separation of CO_2 and CH_4.

3.5. DFT-D calculations

To provide further insight into the interactions between the gas molecules and MOFs, we analyzed the interactions of CO_2 and CH_4 with the framework at the maximum and minimum energy positions when a rigid molecule is moved along a 1D channel (Fig. 4; Figs. S10 and S11 in Appendix A). In the center of the capacious cage space of CuFMOF-c, the interactions between the CO_2 molecules and the MOF mainly occur through weak $O^{\delta-}-H^{\delta+}$ dipole–dipole interactions (C–H···O) with a distance of 3.067–3.082 Å from the hydrogen atom on the aromatic ring (Fig. 4(c)). In addition, the CH_4 molecules form C–H···π bonds with a distance of 3.305 Å from the side of the aromatic ring that is rich in π-electrons (Fig. 4(e)). However, a large energy barrier exists when moving CH_4 and CO_2 through the narrow bottleneck connecting two cages along the *b*-axis direction. In this cramped site, CO_2 was restrained by stronger C–H···O bonds ranging from 2.453 to 3.083 Å (Fig. 4(d)). In contrast, CH_4 was firmly trapped via stronger C–H···π interactions of 3.113–3.218 Å from four surrounding symmetric aromatic rings (Fig. 4(f)), which formed a formidable steric hindrance to prevent the diffusion of CH_4, due to the molecular dimension of CH_4 being comparable to the pore size of the bottleneck structure. A similar phenomenon happened on CuFMOF-a and CuFMOF-b, as depicted in Figs. S10 and S11. These results are
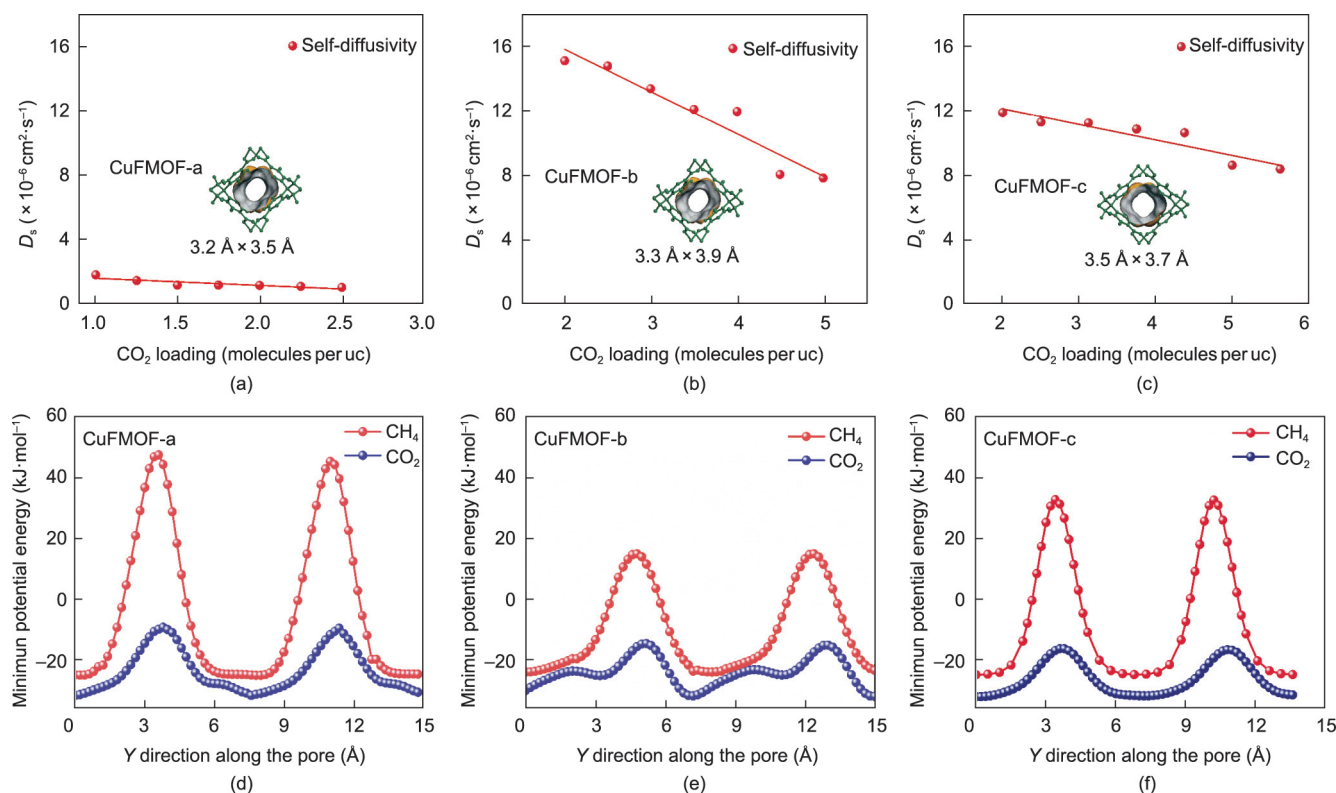
Fig. 3. (a–c) Self-diffusivity (D_s) of CO_2 in (a) CuFMOF-a, (b) CuFMOF-b, and (c) CuFMOF-c at 298 K. (d–e) Minimum potential energy of CH_4 (red) and CO_2 (blue) as a function of position along the 1D channel pore axis in (d) CuFMOF-a, (e) CuFMOF-b, and (f) CuFMOF-c. uc: unit cell.
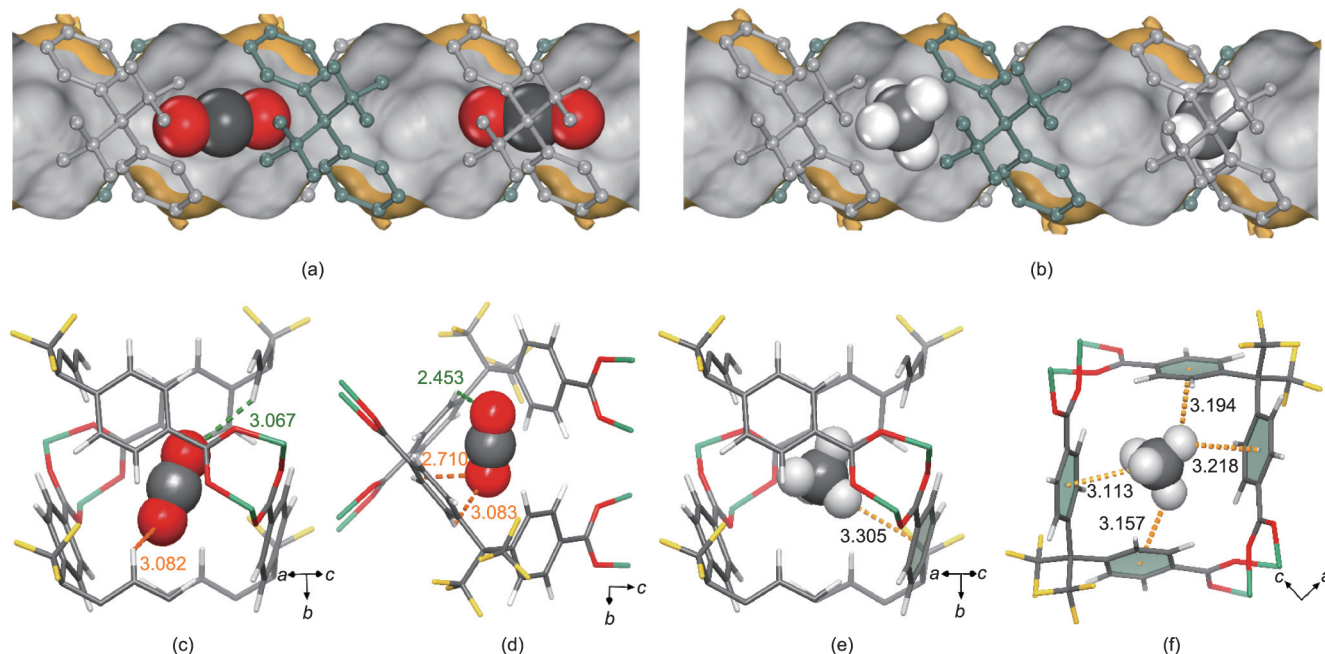
Fig. 4. Scheme of (a) CO_2 and (b) CH_4 molecules moving through the 1D channel. MD was used to calculate the minimum energy binding sites of (c, d) CO_2 and (e, f) CH_4 in the center of the capacious cage space and the smallest bottleneck of the CuFMOF-c structure, which corresponds to the lowest points and the highest points in minimum potential energy diagrams, respectively. The different nets are highlighted in dark green and gray for clarity. Color code: Cu (green), F (yellow), C (gray), O (red).

consistent with those of the diffusion energy barriers, further demonstrating the importance of pore size tuning for diffusion.

4. Conclusions

In summary, we demonstrated the fine-tuning of a geometric structure through a guest solvent-directed strategy in a hydrothermal synthesis that created a subtle discrepancy in the 1D pore aperture of the structure. The highly selective kinetic separation of carbon dioxide and methane over a wide temperature range was realized due to the delicate aperture structure, which periodically outspread and contracted the cross-section of the channel, thereby allowing the entrance of CO_2 but severely hindering the diffusion of CH_4. Ultrahigh kinetic selectivity and equilibrium-kinetic combined selectivity were achieved on CuFMOF-c, surpassing most top-performing adsorbents. This work not only offers a strategy for fine-tuning the host structure but also indicates that an appropriate pore size is a critical step for efficient kinetic separation, providing important clues for the kinetic separation of other gas mixtures with close size and structural similarity.

Compliance with ethics guidelines

Dan Lai, Fuqiang Chen, Lidong Guo, Lihang Chen, Jie Chen, Qiwei Yang, Zhiguo Zhang, Yiwen Yang, Qilong Ren, and Zongbi Bao declare that they have no conflict of interest or financial conflicts to disclose.

Data availability statement

All crystallographic data are available free of charge from the Cambridge Crystallographic Data Centre. The data shown in the plots and those that support the findings of this study are available from the corresponding author on reasonable request.

CIF data for CuFMOF-a (CCDC number: 232689).
CIF data for CuFMOF-b (CCDC number: 1872560).
CIF data for CuFMOF-c (CCDC number: 2004270).

Appendix A. Supplementary material

Supplementary data to this article can be found online at https://doi.org/10.1016/j.eng.2022.03.022.

References

[1] US Energy Information Administration. International energy outlook 2017. Washington, DC: US Energy Information Administration; 2017.
[2] Saha D, Grappe HA, Chakraborty A, Orkoulas G. Postextraction separation, on-board storage, and catalytic conversion of methane in natural gas: a review. Chem Rev 2016;116(19):11436–99.
[3] Connolly BM, Aragones-Anglada M, Gandara-Loe J, Danaf NA, Lamb DC, Mehta JP, et al. Tuning porosity in macroscopic monolithic metal–organic frameworks for exceptional natural gas storage. Nat Commun 2019; 10(1):2345.
[4] Chen FQ, Zhang ZG, Yang QW, Yang YW, Bao ZB, Ren QL. Microporous carbon adsorbents prepared by activating reagent-free pyrolysis for upgrading low-quality natural gas. ACS Sustain Chem Eng 2020;8(2):977–85.
[5] Saleman TL, Li G, Rufford TE, Stanwix PL, Chan KI, Huang SH, et al. Capture of low grade methane from nitrogen gas using dual-reflux pressure swing adsorption. Chem Eng J 2015;281:739–48.
[6] Chen FQ, Wang JW, Guo LD, Huang XL, Zhang ZG, Yang QW, et al. Carbon dioxide capture in gallate-based metal–organic frameworks. Sep Purif Technol 2022;292:121031.
[7] Al-Amri A, Zahid U. Design modification of acid gas cleaning units for an enhanced performance in natural gas processing. Energy Fuels 2020;34 (2):2545–52.
[8] Lin RB, Li L, Alsalme A, Chen B. An ultramicroporous metal–organic framework for sieving separation of carbon dioxide from methane. Small Struct 2020;1 (3):2000022.

[9] Cui H, Ye Y, Liu T, Alothman ZA, Alduhaish O, Lin RB, et al. Isoreticular microporous metal–organic frameworks for carbon dioxide capture. Inorg Chem 2020;59(23):17143–8.

[10] Belmabkhout Y, Bhatt PM, Adil K, Pillai RS, Cadiau A, Shkurenko A, et al. Natural gas upgrading using a fluorinated MOF with tuned H₂S and CO₂ adsorption selectivity. Nat Energy 2018;3:1059–66. Corrected in: Nat Energy 2019;4:83.

[11] Mao VY, Milner PJ, Lee JH, Forse AC, Kim EJ, Siegelman RL, et al. Cooperative carbon dioxide adsorption in alcoholamine- and alkoxyalkylamine-functionalized metal–organic frameworks. Angew Chem Int Ed Engl 2020;59 (44):19468–77.

[12] Xiang S, He Y, Zhang Z, Wu H, Zhou W, Krishna R, et al. Microporous metal–organic framework with potential for carbon dioxide capture at ambient conditions. Nat Commun 2012;3(1):954.

[13] Li JR, Yu J, Lu W, Sun LB, Sculley J, Balbuena PB, et al. Porous materials with pre-designed single-molecule traps for CO₂ selective adsorption. Nat Commun 2013;4(1):1538.

[14] Jahandar Lashaki M, Khiavi S, Sayari A. Stability of amine-functionalized CO₂ adsorbents: a multifaceted puzzle. Chem Soc Rev 2019;48(12):3320–405.

[15] Reynolds AJ, Verheyen TV, Adeloju SB, Meuleman E, Feron P. Towards commercial scale postcombustion capture of CO₂ with monoethanolamine solvent: key considerations for solvent management and environmental impacts. Environ Sci Technol 2012;46(7):3643–54.

[16] Dutcher B, Fan M, Russell AG. Amine-based CO₂ capture technology development from the beginning of 2013—a review. ACS Appl Mater Interfaces 2015;7(4):2137–48.

[17] Rochelle GT. Amine scrubbing for CO₂ capture. Science 2009;325 (5948):1652–4.

[18] Siegelman RL, Milner PJ, Kim EJ, Weston SC, Long JR. Challenges and opportunities for adsorption-based CO₂ capture from natural gas combined cycle emissions. Energy Environ Sci 2019;12(7):2161–73.

[19] Chen F, Ding J, Guo K, Yang L, Zhang Z, Yang Q, et al. CoNi alloy nanoparticles embedded in metal–organic framework-derived carbon for the highly efficient separation of xenon and krypton via a charge-transfer effect. Angew Chem Int Ed Engl 2021;60(5):2431–8.

[20] Chen F, Lai D, Guo L, Wang J, Zhang P, Wu K, et al. Deep desulfurization with record SO₂ adsorption on the metal–organic frameworks. J Am Chem Soc 2021;143(24):9040–7.

[21] Godfrey HGW, da Silva I, Briggs L, Carter JH, Morris CG, Savage M, et al. Ammonia storage by reversible host–guest site exchange in a robust metal–organic framework. Angew Chem Int Ed Engl 2018;57(45):14778–81.

[22] Zhang L, Li L, Hu E, Yang L, Shao K, Yao L, et al. Boosting ethylene/ethane separation within copper(I)-chelated metal–organic frameworks through tailor-made aperture and specific π-complexation. Adv Sci 2020;7 (2):1901918.

[23] Wang Y, Jia X, Yang H, Wang Y, Chen X, Hong AN, et al. A strategy for constructing pore-space-partitioned MOFs with high uptake capacity for C₂ hydrocarbons and CO₂. Angew Chem Int Ed Engl 2020;59(43):19027–30.

[24] Ye ZM, Zhang XW, Liao PQ, Xie Y, Xu YT, Zhang XF, et al. A hydrogen-bonded yet hydrophobic porous molecular crystal for molecular-sieving-like separation of butane and isobutane. Angew Chem Int Ed Engl 2020;59 (51):23322–8.

[25] Cui H, Xie Y, Ye Y, Shi Y, Liang B, Chen B. An ultramicroporous metal–organic framework with record high selectivity for inverse CO₂/C₂H₂ separation. Bull Chem Soc Jpn 2021;94(11):2698–701.

[26] Kong XJ, Li JR. An overview of metal–organic frameworks for green chemical engineering. Engineering 2021;7(8):1115–39.

[27] Chen FQ, Huang XL, Guo KQ, Yang L, Sun HR, Xia W, et al. Molecular sieving of propylene from propane in metal–organic framework-derived ultramicroporous carbon adsorbents. ACS Appl Mater Interfaces 2022;14 (26):30443–53.

[28] Chen FQ, Huang XL, Yang L, Zhang ZG, Yang QW, Yang YW, et al. Boosting xenon adsorption with record capacity in microporous carbon molecular sieves. Sci China Chem 2023;66:601–10.

[29] Chen FQ, Guo KQ, Huang XL, Zhang ZG, Yang QW, Yang YW, et al. Extraction of propane and ethane from natural gas on ultramicroporous carbon adsorbent with record selectivity. Sci China Mater 2023;66:319–26.

[30] Huang XL, Chen FQ, Sun HR, Xia W, Zhang ZG, Yang QW, et al. Separation of perfluorinated electron specialty gases on microporous carbon adsorbents with record selectivity. Sep Purif Technol 2022;292:121059.

[31] Rozyyev V, Yavuz CT. An all-purpose porous cleaner for acid gas removal and dehydration of natural gas. Chem 2017;3(5):719–21.

[32] Dogan NA, Ozdemir E, Yavuz CT. Direct access to primary amines and particle morphology control in nanoporous CO₂ sorbents. ChemSusChem 2017;10 (10):2130–4.

[33] Furukawa H, Cordova KE, O'Keeffe M, Yaghi OM. The chemistry and applications of metal–organic frameworks. Science 2013;341(6149):1230444.

[34] Mofarahi M, Gholipour F. Gas adsorption separation of CO₂/CH₄ system using zeolite 5A. Micropor Mesopor Mat 2014;200:1–10.

[35] Jayaraman A, Chiao AS, Padin J, Yang RT, Munson CL. Kinetic separation of methane/carbon dioxide by molecular sieve carbons. Sep Sci Technol 2002;37 (11):2505–28.

[36] Cavenati S, Grande CA, Rodrigues AE. Upgrade of methane from landfill gas by pressure swing adsorption. Energy Fuels 2005;19(6):2545–55.

[37] Mohamed AR, Mohammadi M, Darzi GN. Preparation of carbon molecular sieve from lignocellulosic biomass: a review. Renew Sustain Energy Rev 2010;14(6):1591–9.

[38] Yamane Y, Tanaka H, Miyahara MT. In silico synthesis of carbon molecular sieves for high-performance air separation. Carbon 2019;141:626–34.

[39] Cai J, Qi J, Yang C, Zhao X. Poly(vinylidene chloride)-based carbon with ultrahigh microporosity and outstanding performance for CH₄ and H₂ storage and CO₂ capture. ACS Appl Mater Interfaces 2014;6(5):3703–11.

[40] Ji Z, Wang HZ, Canossa S, Wuttke S, Yaghi OM. Pore chemistry of metal–organic frameworks. Adv Funct Mater 2020;30(41):2000238.

[41] Dou Y, Zhang W, Kaiser A. Electrospinning of metal–organic frameworks for energy and environmental applications. Adv Sci 2020;7(3):1902590.

[42] Liu W, Yin R, Xu X, Zhang L, Shi W, Cao X. Structural engineering of low-dimensional metal–organic frameworks: synthesis, properties, and applications. Adv Sci 2019;6(12):1802373.

[43] Liu Y, Liu G, Zhang C, Qiu W, Yi S, Chernikova V, et al. Enhanced CO₂/CH₄ separation performance of a mixed matrix membrane based on tailored MOF-polymer formulations. Adv Sci 2018;5(9):1800982.

[44] Yilmaz G, Peh SB, Zhao D, Ho GW. Atomic- and molecular-level design of functional metal–organic frameworks (MOFs) and derivatives for energy and environmental applications. Adv Sci 2019;6(21):1901129.

[45] Bao ZB, Chang GG, Xing HB, Krishna R, Ren QL, Chen BL. Potential of microporous metal–organic frameworks for separation of hydrocarbon mixtures. Energy Environ Sci 2016;9(12):3612–41.

[46] Feng L, Day GS, Wang KY, Yuan S, Zhou HC. Strategies for pore engineering in zirconium metal–organic frameworks. Chem 2020;6(11):2902–23.

[47] Li LB, Lin RB, Wang XQ, Zhou W, Jia LT, Li JP, et al. Kinetic separation of propylene over propane in a microporous metal–organic framework. Chem Eng J 2018;354:977–82.

[48] Ding Q, Zhang Z, Yu C, Zhang P, Wang J, Cui X, et al. Exploiting equilibrium-kinetic synergetic effect for separation of ethylene and ethane in a microporous metal–organic framework. Sci Adv 2020;6(15):eaaz4322.

[49] Krause S, Hosono N, Kitagawa S. Chemistry of soft porous crystals: structural dynamics and gas adsorption properties. Angew Chem Int Ed Engl 2020;59 (36):15325–41.

[50] Kundu T, Wahiduzzaman M, Shah BB, Maurin G, Zhao D. Solvent-induced control over breathing behavior in flexible metal–organic frameworks for natural-gas delivery. Angew Chem Int Ed Engl 2019;58(24):8073–7.

[51] Li YP, Wang Y, Xue YY, Li HP, Zhai QG, Li SN, et al. Ultramicroporous building units as a path to bi-microporous metal–organic frameworks with high acetylene storage and separation performance. Angew Chem Int Ed Engl 2019;58(38):13590–5.

[52] Lv XL, Feng L, Wang KY, Xie LH, He T, Wu W, et al. A series of mesoporous rare-earth metal–organic frameworks constructed from organic secondary building units. Angew Chem Int Ed Engl 2021;60(4):2053–7.

[53] Li X, Wang J, Bai N, Zhang X, Han X, da Silva I, et al. Refinement of pore size at sub-angstrom precision in robust metal–organic frameworks for separation of xylenes. Nat Commun 2020;11(1):4280.

[54] Chanut N, Ghoufi A, Coulet MV, Bourrelly S, Kuchta B, Maurin G, et al. Tailoring the separation properties of flexible metal–organic frameworks using mechanical pressure. Nat Commun 2020;11(1):1216.

[55] Lee CY, Bae YS, Jeong NC, Farha OK, Sarjeant AA, Stern CL, et al. Kinetic separation of propene and propane in metal–organic frameworks: controlling diffusion rates in plate-shaped crystals via tuning of pore apertures and crystallite aspect ratios. J Am Chem Soc 2011;133(14):5228–31.

[56] Lyndon R, You WQ, Ma Y, Bacsa J, Gong YT, Stangland EE, et al. Tuning the structures of metal–organic frameworks via a mixed-linker strategy for ethylene/ethane kinetic separation. Chem Mater 2020;32(9):3715–22.

[57] Gu C, Hosono N, Zheng JJ, Sato Y, Kusaka S, Sakaki S, et al. Design and control of gas diffusion process in a nanoporous soft crystal. Science 2019;363 (6425):387–91.

[58] Pan L, Sander MB, Huang X, Li J, Smith M, Bittner E, et al. Microporous metal organic materials: promising candidates as sorbents for hydrogen storage. J Am Chem Soc 2004;126(5):1308–9.

[59] Metropolis N, Rosenbluth AW, Rosenbluth MN, Teller AH, Teller E. Equation of state calculations by fast computing machines. J Chem Phys 1953;21 (6):1087–92.

[60] Martin MG, Siepmann JI. Transferable potentials for phase equilibria. 1. United-atom description of n-alkanes. J Phys Chem B 1998;102(14):2569–77.

[61] Harris JG, Yung KH. Carbon dioxide's liquid-vapor coexistence curve and critical properties as predicted by a simple molecular-model. J Phys Chem 1995;99(31):12021–4.

[62] Rappe AK, Casewit CJ, Colwell KS, Goddard III WA, Skiff WM. UFF, a full periodic table force field for molecular mechanics and molecular dynamics simulations. J Am Chem Soc 1992;114(25):10024–35.

[63] Frenkel D, Smit B. Understanding molecular simulation: from algorithms to applications. San Diego: Academic Press; 2002.

[64] Saha D, Bao Z, Jia F, Deng S. Adsorption of CO₂, CH₄, N₂O, and N₂ on MOF-5, MOF-177, and zeolite 5A. Environ Sci Technol 2010;44(5):1820–6.

[65] Ruthven DM. Principles of adsorption and adsorption processes. New York City: Wiley-Interscience; 1984.

[66] Cavenati S, Grande CA, Rodrigues AE. Separation of CH₄/CO₂/N₂ mixtures by layered pressure swing adsorption for upgrade of natural gas. Chem Eng Sci 2006;61(12):3893–906.

[67] Bae YS, Lee CH. Sorption kinetics of eight gases on a carbon molecular sieve at elevated pressure. Carbon 2005;43(1):95–107.

[68] Liu J, Liu Y, Kayrak Talay D, Calverley E, Brayden M, Martinez M. A new carbon molecular sieve for propylene/propane separations. Carbon 2015;85:201–11.

[69] Watanabe T, Keskin S, Nair S, Sholl DS. Computational identification of a metal organic framework for high selectivity membrane-based CO_2/CH_4 separations: $Cu(hfipbb)(H_2hfipbb)_{0.5}$. Phys Chem Chem Phys 2009; 11(48):11389–94.